Ocean Water Clarity and the Ocean General Circulation in a Coupled Climate Model

ANAND GNANADESIKAN AND WHIT G. ANDERSON

NOAA/Geophysical Fluid Dynamics Laboratory, and Princeton University, Princeton, New Jersey

(Manuscript received 11 October 2007, in final form 17 July 2008)

ABSTRACT

Ocean water clarity affects the distribution of shortwave heating in the water column. In a one-dimensional time-mean sense, increased clarity would be expected to cool the surface and heat subsurface depths as shortwave radiation penetrates deeper into the water column. However, wind-driven upwelling, boundary currents, and the seasonal cycle of mixing can bring water heated at depth back to the surface. This warms the equator and cools the subtropics throughout the year while reducing the amplitude of the seasonal cycle of temperature in polar regions. This paper examines how these changes propagate through the climate system in a coupled model with an isopycnal ocean component focusing on the different impacts associated with removing shading from different regions. Increasing shortwave penetration along the equator causes warming to the south of the equator. Increasing it in the relatively clear gyres off the equator causes the Hadley cells to strengthen and the subtropical gyres to shift equatorward. Increasing shortwave penetration in the less clear regions overlying the oxygen minimum zones causes the cold tongue to warm and the Walker circulation to weaken. Increasing shortwave penetration in the high-latitude Southern Ocean causes an increase in the formation of mode water from subtropical water. The results suggest that more attention be paid to the processes distributing heat below the mixed layer.

Introduction

If ocean water were perfectly clear, solar radiation in the blue and near-UV bands would penetrate to great depths with *e*-folding scales exceeding 50 m (Morel 1988; Morel et al. 2007). In general, however, the depth of penetration is much shallower than this (Jerlov 1976) due to the presence of phytoplankton pigments, colored dissolved organic matter, and scatterers such as plankton, bacteria, viruses, and suspended particles. This paper considers how the additional shortwave absorption represented by these substances affects the large-scale circulation of the ocean, and how this answer depends on where it is located.

One would expect that decreasing water clarity would result in more trapping of radiation near the surface, increasing surface temperatures, and cooling the deep. A number of authors (Lewis et al. 1990; Stramska and Dickey 1993; Siegel et al. 1995; Strutton and Chavez 2004) have presented one-dimensional analyses demonstrating that changing penetration depths could have a significant impact on the temporal evolution of the mixed layer. More complex models, however, show a more complicated picture. A series of studies with ocean-only models (Nakamoto et al. 2001; Sweeney et al. 2005; Manizza et al. 2005) found that increasing water clarity *increased* the surface temperatures in the cold tongue by up to 1.2°C, with very small changes in sea surface temperature away from this region. This is the opposite of the response that would be expected from a one-dimensional balance. Sweeney et al. (2005) argued that the reason for this change was a decrease in the advective cooling associated with the cold tongue, resulting both from a warming of deeper upwelling water and a reduction of the rate at which cold water is upwelled. The changes in surface temperature occur almost immediately, as do those in upwelling flux. Because of this, Sweeney et al. (2005) argued that it was the relatively fast changes in mixed layer depth, which in turn determines what fraction of the Ekman upwelling is supplied by warm surface waters as opposed to cooler thermocline waters, that governs the temperature response.

There are reasons to believe that ocean water clarity has changed in the past. Paleoproductivity estimates

Corresponding author address: Anand Gnanadesikan, Forrestal Campus, Princeton University, 201 Forrestal Road, Princeton, NJ 08540.
E-mail: anand.gnanadesikan@noaa.gov

DOI: 10.1175/2008JPO3935.1

(Paytan and Griffith 2007) suggest that significant (up to a factor of 5) changes in particle export occur in a number of cores, implying large changes in chlorophyll concentration at these locations. Karl et al. (2001) suggest that chlorophyll concentrations at station ALOHA could have doubled between the 1950s and the present. On even shorter time scales, analysis of interannual variability in the Sea-viewing Wide Field-of-View Sensor (SeaWiFS) chlorophyll-*a* retrievals from 1998 to 2004 (McClain et al. 2004) shows that even over this relatively small period, for over 40% of the ocean the observed range of chlorophyll is more than 40% of the mean value. A particularly striking feature is the high variability occurring along the boundary between the high and low chlorophyll zones. Polovina et al. (2008) note that there are trends in the SeaWiFS dataset, suggesting that the very clear regions are expanding.

Whether changes in SST produced by changing ocean color can have a major impact on the climate system will be determined by whether or not they are amplified or damped by the atmosphere. Shell et al. (2003) suggested that the initial response of the atmosphere should be to increase the SST perturbations, as they would be expected to trigger Bjerknes-type feedbacks. However, a result showing that the initial response to a climate perturbation will amplify does not necessarily imply that the long-term response will be large. As the El Niño–Southern Oscillation system shows, both positive and negative feedbacks act on changes in equatorial circulation. As a result, a long-term mean El Niño–like perturbation will be damped if the reduction in upwelling results in a decrease in the volume of light water and a shoaling of the thermocline (Federov et al. 2006).

Two lines of research have examined this question with coupled climate models. One line, represented by Murtugudde et al. (2002) and Ballabrera-Poy et al. (2007), uses a hybrid coupled model to examine the impacts of changing the penetration from a uniform penetration depth of 17 m to one based on chlorophyll estimated using the Coastal Zone Color Scanner (CZCS) satellite. Timmermann and Jin (2002) and Marzeion et al. (2005) extended these results to look at the impact of interactive chlorophyll. These papers allow for changes in the mean state of the ocean but ignore atmospheric thermodynamic feedbacks and, in general, find relatively small changes in such features as sea surface currents and overturning, though not necessarily small changes in tropical variability. Because of the spatial structure of the observed chlorophyll field, the perturbation that is used in these simulations often results in a decrease in water clarity and shortwave penetration at the equator and an increase off the equator in subtropical gyres relative to the fixed-attenuation scale controls.

A second line of research has examined the impact of changing shortwave absorption in a fully coupled climate model. Wetzel et al. (2006) examine this effect in the Max Planck Institute model, changing the *e*-folding scale from 11 m to a spatially varying field. They find an average increase in surface temperatures in the cold tongue of 0.5°C with maximum changes between 0.6° and 1°C. Lengaigne et al. (2007) also use a full coupled climate model and examine the difference between using a constant attenuation depth and predicted chlorophyll concentrations. They find a warming of the cold tongue of about 1°C and very weak off-equatorial cooling. As with the hybrid models, their simulated chlorophyll fields also result in a decrease in penetration along the equator and an increase in penetration in the gyres relative to the constant-attenuation control (and interestingly also relative to observations). The results of Sweeney et al. (2005) suggest that this could produce some compensation between increasing upwelling due to increased attenuation near the equator (which would cool the cold tongue) and increasing subsurface temperatures through deeper penetration of shortwave radiation off the equator (which would warm the cold tongue). None of these coupled simulations has looked at the *total* impact of absorbers and scatterers, as the ''clear'' water controls used still absorb a great deal. It is thus possible that all of these coupled simulations have underestimated the importance of ocean water clarity on the large-scale circulation due to their experimental design.

In recent work (Anderson et al. 2007) we examined the impact of removing *all* of the additional absorption associated with dissolved and suspended substances in a coupled climate model, thus increasing the penetration depth of shortwave radiation everywhere. We found that this warmed the cold tongue by up to 1.8°C and cooled some extratropical regions by about a comparable amount (approximately 2–3 times the signal seen by Wetzel et al. 2006 and Lengaigne et al. 2007). Following Sweeney et al. (2005), we also highlighted the importance of shortwave absorption in the clear centers of the subtropical gyres, as compared to absorption right along the equator.

This paper extends these results to examine three main questions. First, we examine how these changes in surface temperature affect the ocean circulation as a whole, both directly and through changing the wind field. Second, we examine the degree to which this response is linear in chlorophyll concentration. Finally, we examine in detail how different regions on and off the equator have different impacts on the climate system. In addition to providing information about possible biological–physical couplings, this work reveals some

interesting sensitivities to the distribution of heating within the water column that may have implications for the representation of physical mixing in coupled climate models.

2. Model description

The atmospheric and land components of the model are identical to those used for the CM2.1 global coupled climate model developed for the Fourth Assessement Report (AR4) of the Intergovernmental Panel on Climate Change and reported in Delworth et al. (2006). The atmosphere is built around a 24-level, 2° × 2.5° finite volume core with state-of-the-art representations of radiation, convection, and gravity wave drag. The land model is the LM2 model based on the work of Milly and Shmakin (2002), which fixes land properties such as albedo, surface roughness, and stomatal resistance (which controls evapotranspiration) based on currently observed land types. The model has one of the better atmospheric simulations in the AR4 dataset (Reichler and Kim 2008) and when coupled has been found to exhibit a reasonable simulation of El Niño and its feedbacks for both a level-coordinate ocean model (Van Oldenburgh et al. 2005) and an isopycnal ocean model (Anderson et al. 2008, manuscript submitted to *Ocean Sci.*)

The primary difference between these runs and those done for the Fourth Assessment Report is the ocean model. The AR4 models used the level coordinate Modular Ocean Model, version 4, code with shortwave absorption based on the observed distribution of chlorophyll as described in Sweeney et al. (2005). The ocean model used in our simulations is the isopycnal layer model of Hallberg (2005). One key feature of this model is that it has essentially no numerical diapycnal mixing, allowing for clean attribution of changes in heat redistribution at depth (Harrison and Hallberg 2008). Additionally, isopycnal models are able to more accurately resolve and simulate the physics of overflows (Winton et al. 1998). The model was configured with 48 interior isopycnal layers, which strive to follow a set of target densities in addition to a four-layer mixed layer/buffer layer in which densities are free to vary. The code includes a nonlinear equation of state and Richardson-number-dependent shear mixing. The impact of unresolved mesoscale eddies is parameterized using a biharmonic Smagorinsky viscosity and along-isopycnal mixing of both tracers and interface height [corresponding to the Gent and McWilliams(1990) parameterization of eddy Stokes drift in level-coordinate models]. A constant coefficient of 900 $m^2\ s^{-1}$ is used for both terms.

A key difference between the model used in these simulations and previous instantations of the isopycnal model is that we incorporate the two-band shortwave penetration scheme of Manizza et al. (2005), which is a renanalysis of the data of Morel (1988) that permits very low chlorophyll concentrations. As the near-infrared and red–yellow bands of light have short *e*-folding depths (less than 5 m) and our mixed layer in these runs has a minimum depth of 10 m, these bands are simply treated as a surface flux of heat. The blue–green band (with wavelengths less than 550 nm) is allowed to penetrate, following a profile given by

$$I(z) = I_{\mathrm{bg}} e^{-k_{\mathrm{bg}} z} = 0.21 I_0 \mathrm{e}^{-k_{\mathrm{bg}} z} \tag{1a}$$

$$k_{\mathrm{bg}} = 0.0232 + 0.074 \times \mathrm{chl}^{0.674}, \tag{1b}$$

where I_0 is the total absorbed shortwave radiation (21% of which is taken to be blue–green) and chl is the concentration of chlorophyll-*a* in mg chl m^{-3}. Thus, if the chlorophyll is set to 0, blue–green light has an *e*-folding depth of 43 m, while at values of 0.2 mg chl m^{-3} the *e*-folding depth is ~20 m. In the base state of the model, the chlorophyll concentrations are taken from the non–El Niño SeaWiFS climatology developed by Sweeney et al. (2005), which is currently distributed with the Geophysical Fluid Dynamics Laboratory (GFDL) ocean codes. As seen in Fig. 1a, this results in *e*-folding depths exceeding the 23 m associated with Jerlov Type I waters over much of the subtropical gyres.

To understand differences between our results and previous simulations, it is important to compare the perturbation in heating rates at different depths. An alternative shortwave penetration parameterization is given by Moore et al. (2002) and Wetzel et al. (2006), for which $I_{\mathrm{bg}} = 0.5 I_0$ and

$$k_{\mathrm{bg}} = 0.04 + 0.03\mathrm{chl}. \tag{2}$$

As shown in Fig. 1b, this produces much less of a range in penetration depth over most of the ocean. Figures 1c,d compare the annual average heating rate in °C yr^{-1} caused by shortwave heating at two depths (given I_0 = 200 W m^{-2}) using a number of published penetration parameterizations. We can get an estimate of the size of the perturbation studied in a given work by looking at the difference between heating rates associated with two parameterizations. At 100 m, the change in heating studied by Wetzel et al. (2006) is similar to the change between the lowest dashed line and the solid line with triangles, or about 0.4°C yr^{-1}. This is slightly smaller than the ~0.55°C yr^{-1} difference between the Manizza et al. (2005) parameterization (solid line) and our representation of clear water (top dashed line), although

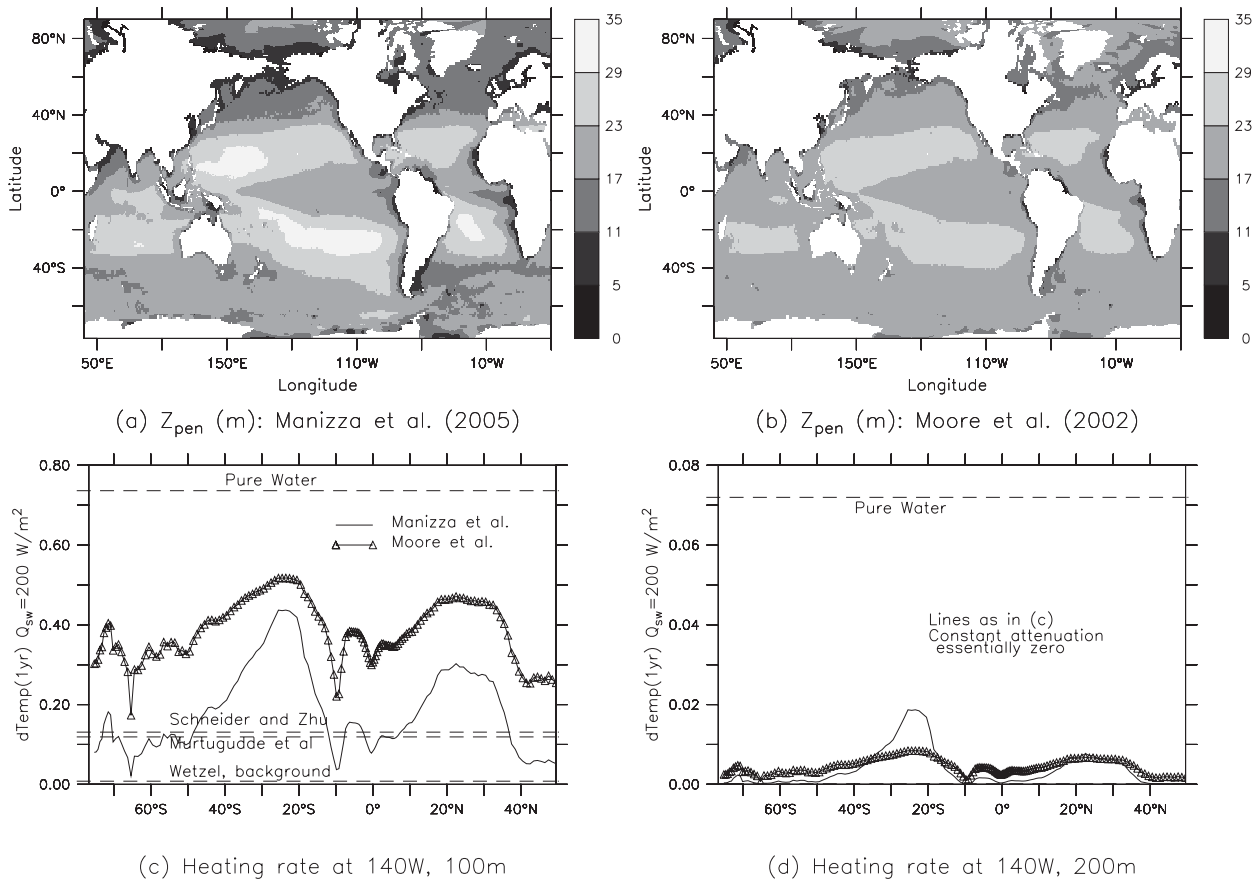

FIG. 1. Structure of chlorophyll-dependent shortwave heating. (a) Penetration depths for the Manizza et al. (2005) scheme using a SeaWiFS-based chlorophyll-*a* climatology. Contours between 5 and 23 m correspond to values associated with previous work. Wetzel et al. (2006) used a baseline of 11 m, Murtugudde et al. (2002) used a baseline of 17 m, and Jerlov (1976) Type I water has an *e*-folding scale of 23 m. (b) Penetration depth for the scheme of Moore et al. (2002). (c) Heating rates (°C yr^{-1}) for an incoming solar radiation of 200 W m^{-2} (c) at 100 m and (d) at 200 m depth along a section at 140°W.

our model will see much more spatial variability in heating rate than did Wetzel et al. Note that despite the smaller penetration depth the background heating rate is larger using Moore et al. (2002) because the fraction of penetrating radiation is much higher. Perturbations in shortwave heating in a number of other studies are also represented on this plot. Schneider and Zhu (1998), in a pioneering study on the impact of shortwave heating, introduced a 15-m *e*-folding depth for solar radiation. At 100 m, this corresponds to a change in heating of 0.13°C yr^{-1}—significantly smaller than the perturbation that we employ. Murtugudde et al. (2002) examine the difference between a 17-m *e*-folding depth and a spatially dependent penetration depth. This perturbation will have the same general shape as the difference between the dashed line at 0.11°C yr^{-1} and our control case, O(0–0.3°C yr^{-1}) depending on the location. Thus, when we remove chlorophyll altogether, we are producing a significantly larger change in solar heating at 100 m over a broader latitudinal range than in any of these simulations except for Wetzel et al. (2006).

At 200 m, this difference is even more pronounced (Fig. 1d). Replacing our chlorophyll-dependent parameterization with clear water produces a much larger impact on subsurface heating (0.07°C yr^{-1}) than any of the previous coupled model studies, which at most involve a subsurface warming 10%–15% as large. While 0.07°C yr^{-1} may seem insignificant, it can result in significant temperature perturbations when integrated over the decadal time scales associated with the subtropical gyres.

All of the models described herein were initialized from a modern January climatology based on the *World Ocean Atlas* dataset. The concentrations of radiatively active trace gas concentrations are fixed at a 1990 level throughout the simulations so that the runs correspond to the 1990 control runs in the IPCC AR4 model databases. The models all develop a very strong La Niña in

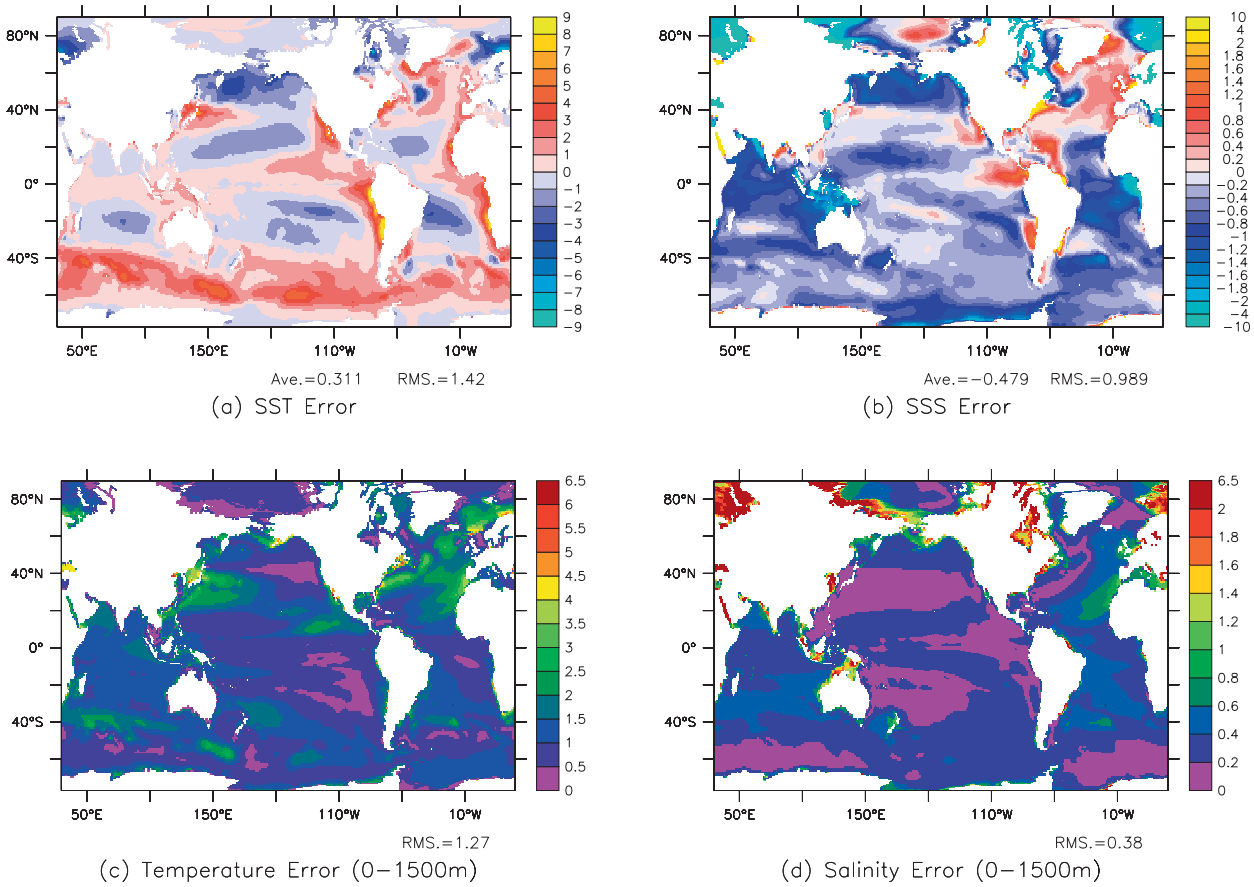

FIG. 2. Errors (compared with the *World Ocean Atlas* regridded to the model grid) in the control simulation averaged over years 200–300: (a) sea surface temperature (°C), (b) sea surface salinity (psu) and rms error in (c) temperature and (d) salinity within 0–1500 m.

the first 20 yr, but afterward are relatively stable as regards their tropical climate. The base state (using the monthly varying version of the penetration depths in Fig. 1a) is referred to as the *Green* run. The Green simulation is comparable to other models run as part of the AR4 process. The rms sea surface temperature error (Fig. 2a) from years 200–300 of the control run is 1.42°C, slightly less than for the GFDL CM2.0 model and about 0.2°C greater than for the CM2.1 model (Table 1), which are among the top-performing models in the IPCC Fourth Assessment Report. The MPI model of Wetzel et al. (2006) is comparable to CM2.1 with a rms SST error of 1.27°C and the L'Institut Pierre-Simon Laplace (IPSL) model used in Lengaigne et al. (2007) has a significantly higher error of 1.97°C. All of these models have comparable errors of about 1°C in the tropics, though regional patterns are somewhat different. An area of particular interest is the Pacific cold tongue, where the Green model has a small positive bias, in marked contrast to the strong negative biases in the CM2 series runs. The pattern of tropical errors is quite well correlated with biases in absorbed surface radiation, reflecting the difficulty in properly simulating low stratus decks and shallow cumulus convection. Rms temperature errors in the top 1500 m in the Green model (Fig. 2c) are lower than in either of the two level-coordinate models—particularly in the Atlantic.

TABLE 1. Control model compared with the two GFDL global coupled climate models run for the AR4: Temperature errors and biases (°C) and salinity errors and biases (psu).

Property	Green (Isopycnal)	CM2.0 (Level)	CM2.1 (Level)
Rms SST error global	1.42	1.49	1.23
90°–30°S	1.58	1.31	1.42
30°S–30°N	1.26	1.05	1.04
30°–90°N	1.62	2.60	1.41
Rms temperature error 0–1500 m	1.31	1.71	1.42
Mean SSS bias	−0.48	−0.43	−0.20
Rms SSS error	0.99	1.04	0.87
Rms salinity error 0–1500 m	0.38	0.37	0.33
SST bias 2°S–2°N, 180°–100°W	0.28	−0.90	−0.70

Salinity errors (Fig. 2b,d) in the Green model are slightly worse than in the CM2 series, possibly because this model has not been subjected to exhaustive tests of how to mix freshwater into the interior at river mouths.

Several perturbations in ocean water clarity were performed. The first (*Blue*) was the largest possible, removing all additional shortwave absorption associated with dissolved and suspended particles. The Blue model was run for 300 years. Additionally, four additional 120-yr runs were made in which the chlorophyll concentration was everywhere reduced by 50% (*Half*), set to zero in the Pacific within 30° of the equator when it was less than 0.2 mg m^{-3} (*BLPGyre*), set to zero in the Pacific within 5° of the equator (*BLPEqu*), and set to zero within 30° of the equator in all tropical regions where the average chlorophyll is greater than 0.2 mg m^{-3} (*BLTMarg*). The Half run thus can be used to evaluate the linearity of the system and the BLPEqu run to evaluate the impact of equatorial water clarity. The BLPGyre and BLTMarg runs examine the impact of low-productivity, oligotrophic gyre centers versus the higher-productivity, mesotrophic gyre margins overlying the oxygen minimum zones.

The perturbations that we have made in these runs are quite large. This was done intentionally to set an upper limit on the additional impact of shortwave absorption due to dissolved and suspended material in different regions. As can be seen from Fig. 1, the result is to produce much larger changes in heating at greater depths than in previous coupled simulations—showing that the total impact of dissolved and suspended material may be significantly larger than previously realized.

In addition to the full coupled runs, a number of simulations were made with the ocean component of the model forced by the Coordinated Ocean Reference Experiment winds and heat fluxes with a weak salinity restoring (Griffies et al., ~~2007~~). We focus here on the difference between Green and Blue ocean-only runs.

3. Results

a. SST and wind stress changes

That ocean water clarity has an important impact on sea surface temperature and wind stress~~, as~~ clearly shown in Fig. 3. The net impact on SST of making ocean waters clear—illustrated by the Blue − Green differences in Fig. 3a—is global in extent, with peak values exceeding 4°C and rms differences of 0.6°C. The pattern shows a strong warming in the central Pacific, with cooling off-equator in the subtropical gyres (particularly in the Atlantic), strong cooling at the boundary between the subtropical and subpolar gyres, and warming in the subpolar gyres. The associated wind stress changes have a complicated pattern. Increasing equatorward winds to the north and south of the equator in the central Pacific correspond to a strengthening of the Hadley circulation. Although they cannot be seen in Fig. 3a, there are also westerly wind anomalies of up to 0.02 Pa along the equator, corresponding to a slackening of the easterlies exceeding 1 m s^{-1} between 140°E and 140°W and reaching a maximum of 2.2 m s^{-1} around 160°E. These changes are associated with an ~15% weakening of the Walker circulation. The northern jet stream shows a tendency to shift equatorward. The southern jet stream shows some hint of a shift but also weakens significantly. The changes in mean winds and wind stress seen here are much larger than those seen in Shell et al. (2003), who found maximum changes of 0.8 m s^{-1} along the equator, and Lengaigne et al. (2007), who found a maximum change in wind stress of 0.004 Pa along the equator.

The magnitude of the response to changing chlorophyll is somewhat nonlinear, as might be expected from the exponential dependence of absorption. When the chlorophyll decreases by a factor of 2 (Half run, Fig. 3b), the pattern of the SST response is reasonably similar to that produced by increasing water clarity everywhere (correlation coefficients are high globally and in the central Pacific) but the magnitude is attenuated, reaching only 35%–40% of that seen in Fig. 3a. The wind stresses show similar changes in the equatorial region, but less of a change in the subpolar regions.

As discussed in Anderson et al. (2007), relatively little of the response can be explained by changes in water clarity right along the equator. The pattern of SST change in the BLPEqu simulation (in which all the additional shortwave penetration occurs in the equatorial Pacific, Fig. 3c) is poorly correlated with the global Blue − Green difference. This is true even in the central Pacific, where the largest signals are seen. Essentially, the warming in the eastern Pacific to the south of the equator is the only major feature reproduced. The magnitude of the SST response to changing near-equatorial shortwave penetration is quite small, $O(10\%)$ of the response to setting the water to be clear everywhere.

By contrast, in the BLPGyre run (in which the increased shortwave penetration occurs off-equator in the clear subtropical gyre centers, Fig. 3d) a much more vigorous response with significantly higher correlation to the Blue–Green response is seen. This simulation reproduces the pattern of on-equatorial warming (though weakly), strong off-equatorial cooling, and the shift of the gyre boundary in the North Pacific. The wind stress response, however, is much more confined to the equator than in Blue and does not exhibit the westerly

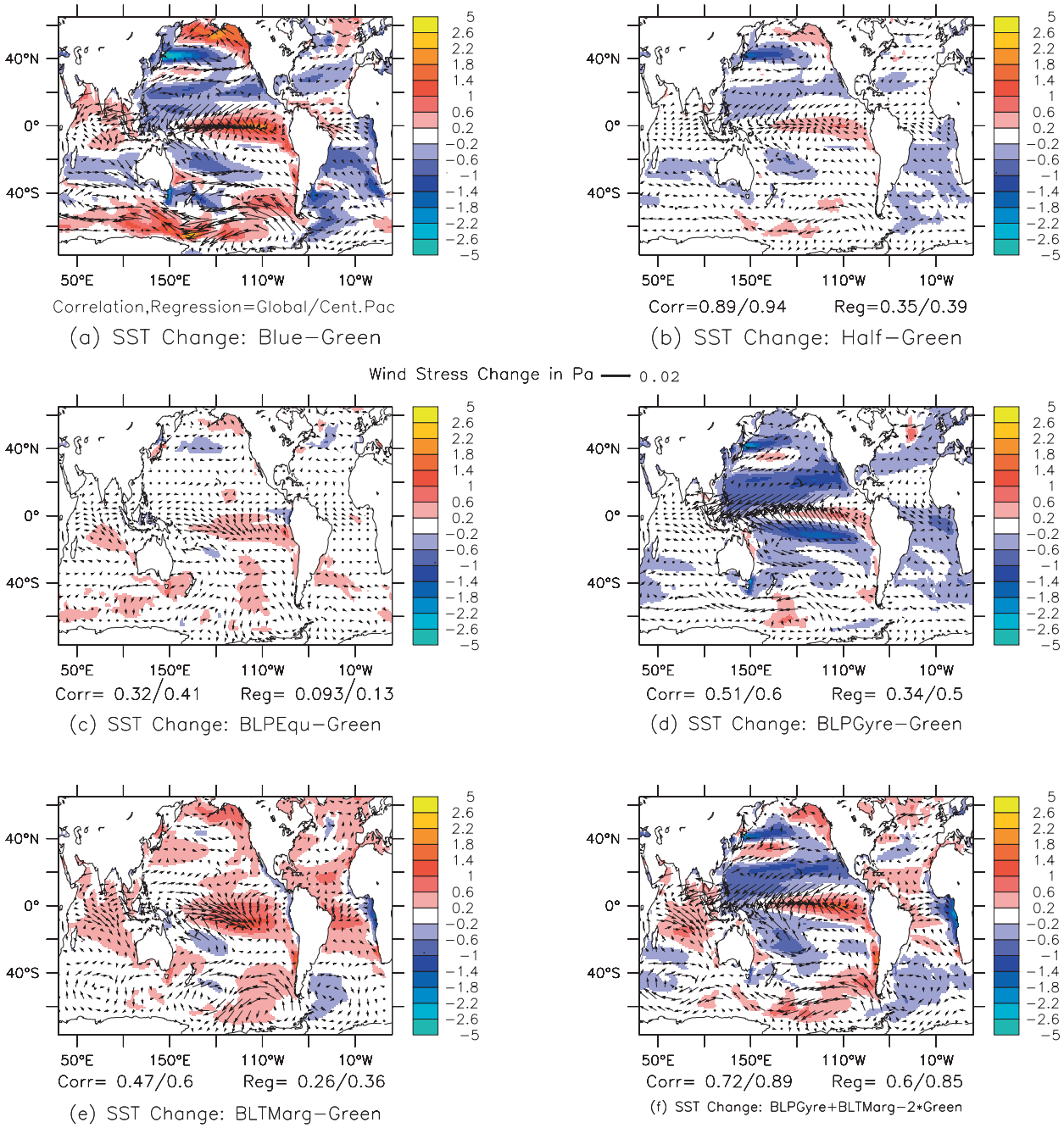

FIG. 3. Sea surface temperature (°C) and wind stress changes from changing ocean water clarity for years 41–120. Numbers show the correlation and regression coefficients for the SST difference vs the Blue − Green difference, enabling evaluation of which regions are most important for producing the changes in the Blue run: First number is for globe, second for tropics. (a) Blue − Green, (b) Half − Green, (c) BLPEqu − Green, (d) BLPGyre − Green, (e) BLTMarg − Green, and (f) (BLTMarg − Green) + (BLPGyre − Green).

anomalies along the equator. Essentially, the Pacific branch of the Hadley cell appears to be sensitive to the water clarity in the gyres.

The BLTMarg simulation (in which the additional penetration occurs in the less-clear eastern portions of the basin, Fig. 3e) shows a quite different pattern, with a general warming over most of the ocean, but particularly strong in the eastern Pacific. The winds follow this warm anomaly, which results in a strengthening of the southern Hadley cell and a strong westerly anomaly

TABLE 2. Regression coefficients (W m^{-2} °C^{-1}) and correlations (in parentheses) between differences in SST (ΔSST) and differences in total air–sea heat fluxes (ΔHF) and net shortwave flux (ΔSW) associated with changes in ocean water clarity. Regressions are broken down by the region over which the perturbation is applied (columns) and the region over which the response is evaluated (rows). Negative values show that atmospheric thermodynamic feedbacks act to damp the SST perturbation (reducing the flux into the ocean if the ocean warms): positive values show that they would reinforce it.

	Blue − Green	BLPGyre − Green	BLTMarg − Green	BLPEqu − Green	Blue − Green ocean only
ΔSST–-ΔHF, Global	−12.5 (−0.62)	−10.8 (−0.55)	−12.0 (−0.52)	−12.4 (−0.48)	−43.1 (−0.89)
ΔSST–ΔHF: 90°–30°S	−11.4 (−0.56)	−13.4 (−0.63)	−7.3 (−0.38)	−11.2 (−0.45)	−44.1 (−0.86)
ΔSST–ΔHF: 30°S–30°N, 80°W–120°E	−13.5 (−0.55)	−7.1 (−0.44)	−25.5 (−0.86)	−12.3 (−0.43)	−47.0 (−0.98)
ΔSST–ΔHF: 30°S–30°N 120°E–80°W	−13.6 (−0.65)	−10.9 (−0.52)	−9.3 (−0.42)	−12.4 (−0.45)	−48.5 (−0.99)
ΔSST–ΔHF: 30°–90°N	−11.9 (−0.70)	−18.0 (−0.82)	−10.0 (−0.50)	−16.9 (−0.71)	−28.5 (−0.81)
ΔSST–ΔSW: Global	−1.2 (−0.10)	−2.0 (−0.15)	−2.6 (−0.21)	−2.3 (−0.16)	
ΔSST–ΔSW: 90°–30°S	2.6 (0.36)	1.1 (0.17)	1.5 (0.18)	1.5 (0.16)	
ΔSST–ΔSW: 30°S–30°N, 80°W–120°E	2.5 (0.18)	0.5 (0.04)	−4.6 (−0.43)	−7.9 (−0.46)	
ΔSST–ΔSW: 30°S–30°N 120°E–80°W	−8.9 (−0.54)	−5.2 (−0.28)	−5.5 (−0.34)	−5.0 (−0.26)	
ΔSST–ΔSW: 30°–90°N	2.7 (0.41)	1.8 (0.30)	2.7 (0.37)	2.4 (0.38)	

along the equator. The Walker circulation appears to be much more sensitive to water clarity above the oxygen minimum zones than to water clarity in the subtropical gyres, while the reverse is true for the Hadley cell.

It is interesting to consider the extent to which the effects of water clarity perturbations are linear in space, by adding the SST change between BLPGyre and Green to that between BLTMarg and Green. If linearity holds, the sum will be similar to the Blue − Green difference except for changes related to high-chlorophyll regions poleward of 30°S and changes in the gyres in other ocean basins. The result (Fig. 3f) is a pattern that has a very high correlation with Blue–Green in the central Pacific, where it reproduces not only most of the spatial pattern but about 85% of the magnitude. Globally, the correlation is significantly lower, as the large warming of the subpolar gyres and cooling of the Atlantic is not reproduced—pointing to the potential importance of chlorophyll and other absorbers in these regions.

These results are very different from the ocean-only simulations presented in Anderson et al. (2007), where the temperature increases are largely limited to the equatorial Pacific. One reason could be that the atmospheric feedbacks are different—a hypothesis that we explore by looking at the relationships between surface air–sea heat fluxes and SST changes (Table 2). The regressions presented in the top row of Table 2 demonstrate that, while the atmosphere in the coupled model acts to damp out SST perturbations, this damping is fairly weak on a global scale with a 1°C warming resulting in an air–sea flux change $O(-10$ W m^{-2} °C^{-1}). The SST changes cannot be directly forced by changes in atmospheric heat flux. However, while correlation coefficients between heat flux and SST change are clearly significant (ranging from −0.48 to −0.62 on a global scale), these numbers are *much* smaller than the $O(-45$ W m^{-2} °C^{-1}) decrease in air–sea heat flux (and correlations of −0.81 to −0.99) seen in the ocean-only calculations. Thus, given the same change in oceanic heat convergence, the coupled model will produce four times the SST change as the ocean-only run. Moreover, in the coupled runs more than half of the spatial variance in SST change is uncorrelated with the change in heat flux and, therefore, is not damped by it.

The results in the bottom half of Table 2 do show that another assumption usually made in ocean-only or hybrid coupled model runs—that of fixed shortwave radiation—is more justifiable. The shortwave feedbacks, in general, damp perturbations in the tropical Pacific (with a 1°C rise in SST resulting in a 5–9 W m^{-2} decrease in absorbed shortwave radiation, though with generally low correlations with the SST change). In the extratropics, a 1°C rise in SST results in a 2–3 W m^{-2} *increase* in absorbed shortwave radiation:Radiative feedbacks on SST changes are weakly positive. Thus, while shortwave biases may cause us to overestimate the importance of chlorophyll in cold shadow zones by allowing too much penetrating radiation to reach the ocean surface, the changes in SST do not greatly enhance the biases in cloudiness.

The water balance over the ocean also changes as the water clarity is changed (Fig. 4). As with temperature, the basic pattern can be seen to consist of two main components. The first pattern, exemplified by BLPGyre, involves increased penetration in the clear gyre centers,

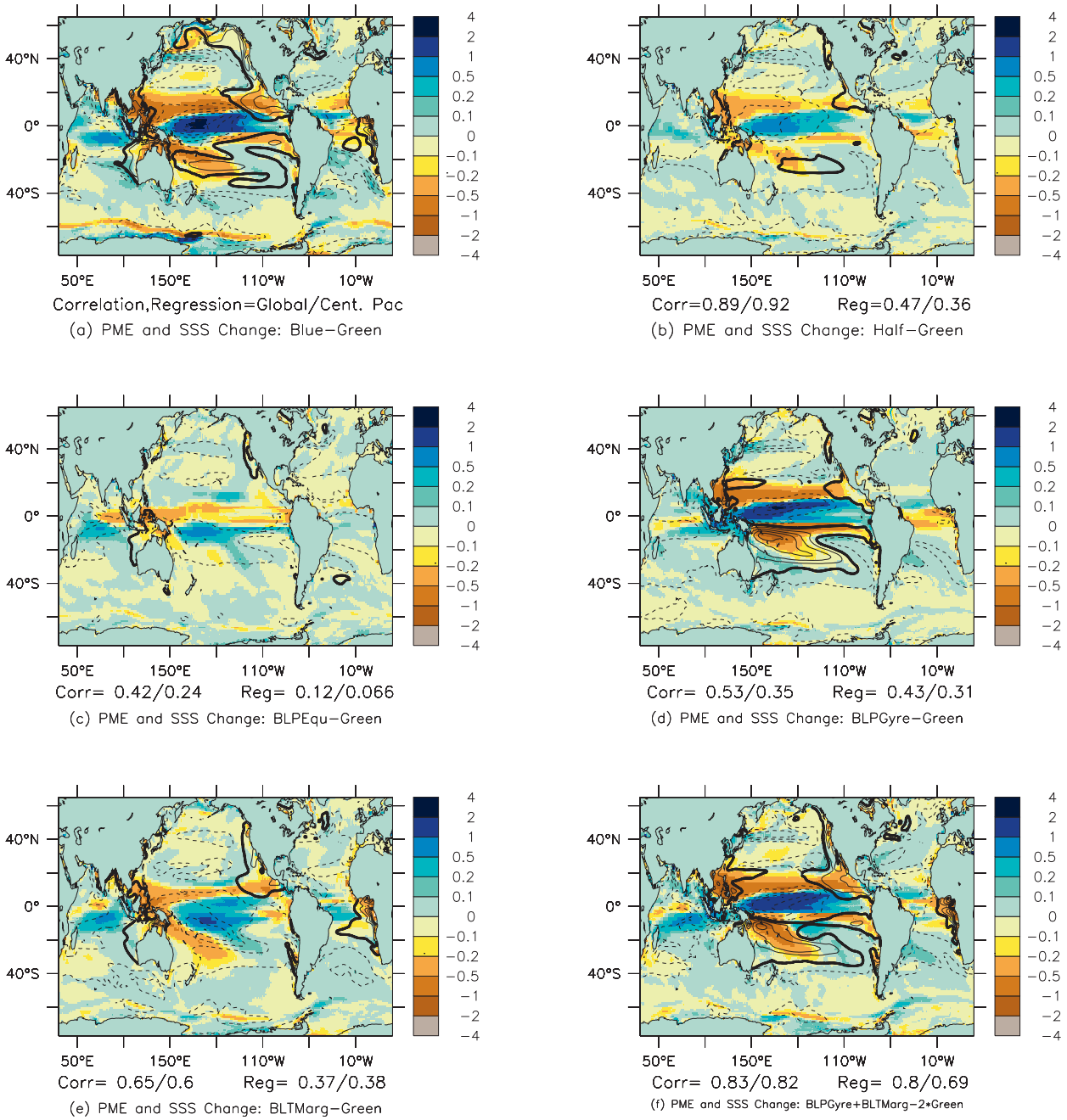

FIG. 4. Precipitation minus evaporation (m yr^{-1}, colors) and surface salinity (contours, interval 0.2 psu, thick solid line corresponds to zero contour, solid lines are positive, dashed lines are negative) changes relative to Green run for years 41–120 of the simulations. Correlation and regression coefficients of the change compared with Blue − Green are shown by the numbers below each plot. (a) Blue − Green, (b) Half − Green, (c) BLPEqu − Green, (d) BLPGyre − Green, (e) BLTMarg − Green, (f) (BLTMarg − Green) + (BLPGyre − Green).

resulting in a strengthening of the Hadley cell (Fig. 4d) and producing lower salinities along the equator and higher salinities off the equator in the center of the subtropical gyres. The other pattern, exemplified by BLTMarg (Fig. 4e), involves increased penetration above the oxygen minimum zones, producing a warming of the cold tongue and an eastward shift of the precipitation into the central Pacific, away from Indonesia. The salinity change associated with this perturbation is largely negative, with maximum freshening of ~0.6 psu over the central Pacific. The zero line in sea surface salinity (SSS) change for BLTMarg–Green does not

correspond to the zero line in precipitation–evaporation change—a large region in the southeast Pacific in which $P - E$ change is positive shows a *decrease* in salinity. This contrasts with the somewhat better correspondence in Blue–Green or BLPGyre–Green. This illustrates how changes in the $P - E$ balances between gyres are much more effective at producing changes in salinity than changes in the $P - E$ balance within gyres where advection homogenizes water properties.

b. Zonal mean temperature, salinity, and age

Having sketched out the changes in surface properties, we now examine the corresponding changes in the structure of the interior ocean. The basic picture in the tropics is one in which increasing penetration of solar radiation leads to a small net cooling of the surface and a large (up to 2.5°C in the Blue run) warming between 100 and 400 m (Fig. 5a). Given that the average age of the waters at 200-m depth is about 20 yr and that the additional heating rate from removing chlorophyll at 200 m is around 0.07°C yr^{-1} (Fig. 1d), such a large change is roughly the right size, as waters coming from above will have experienced higher additional heating rates. These depths also become saltier (Fig. 5c). One of the tracers run in these models was ideal age, which is set to 0 in the mixed layer and increases at 1 yr yr^{-1} below the mixed layer, thus giving a measure of how long it has been since water was in contact with the atmosphere. Differences in ideal age show that increased shortwave penetration makes the water younger in the tropics (Fig. 5e). The response to these changes is not linear in the chlorophyll concentration. The Half run shows about 1/4 of the Blue signal in tropical temperature and salinity and exhibits an even smaller signal in age—much less than the 35%–40% of the SST signal. The importance of shortwave penetration in the off-equatorial gyres is illustrated by the fact that the BLPGyre run has a pattern of change similar to the Blue run between 200 and 400 m in all three fields, although the magnitude of the change is only 20%–40% of that in the Blue run. Additionally, there is considerable penetration of warming below 400 m, with the Blue run showing 0.6°C of warming at 600 m. At these depths none of the other runs shows much of a signal.

These deep changes may be linked to changes in the Southern Ocean. Examination of the temperature fields (Fig. 5b) shows an increase in these same waters in the Blue run. Such changes are not seen in the other simulations, suggesting that high-latitude changes in water clarity may be important. The Blue run also has a significantly fresher surface Southern Ocean (Fig. 5d) and an older middepth Southern Ocean with waters aging by up to 6 yr (Fig. 5f). Both BLPGyre and BLTMarg show qualitatively similar patterns of change in salinity and age, with increasing Southern Ocean stratification in the mean. We will examine this issue in more detail in section 3d when we consider Southern Ocean water mass formation.

c. Linking the changes to transport

The differences between the BLTMarg and BLPGyre runs are quite striking, with the first run producing a net warming over most of the low latitudes and the second producing a net cooling over most of the subtropics. What accounts for the structure of the differences between these runs? Part of the answer can be seen by looking at the structure of heat export from the tropical Pacific. We examine the quantity

$$Q_T^k = \sum_{n=0}^{k} \int_x \rho c_p v_n T_n h_n dx$$

where ρ is the density, c_p the specific heat, v the velocity, h the layer thickness, and T the temperature, summed over layers 1 to k and integrated zonally. Here Q_T^k corresponds to the advective transport of temperature at densities lighter than layer k, converted into petawatts. This diagnostic helps isolate which water masses contribute to the total heat transport. At 23°N in the Pacific (Figs. 6a,b), the Blue and BLPGyre runs show a distinct shift in the layers that transport heat poleward from those associated with the mixed layer to those associated with the upper thermocline. In Blue and BLPGyre, more heat is added to the lower part of the mixed layer, in the gyre interior, where it moves equatorward in the interior of the gyre (cf. the solid blue and green lines in Fig. 6b). Most of this heat is returned in the upper thermocline in the western boundary current (cf. the dashed blue and green lines in Fig. 6b).

By contrast, in the BLTMarg run, the bulk of the heat added below the mixed layer goes into the upper thermocline in the heart of the shadow zones. Luyten et al. (1983) define these regions as locations where isolines of potential vorticity (PV) tend to intersect the eastern boundary rather than connecting with the mixed layer. Their theory also predicts that there should be a minimum in layer thickness (corresponding to a front in PV) along the boundary between the ventilated gyre and the shadow zone. As noted by Gnanadesikan et al. (2007) among others, this boundary is found in both the real world and models, where it corresponds to a location of sharp gradients in PV, oxygen, chlorofluorocarbons, and ideal age—consistent with the idea that water within the shadow zones has limited advective connection to the surface. It is not surprising that heat added to this region is trapped locally. What is surprising, and should make

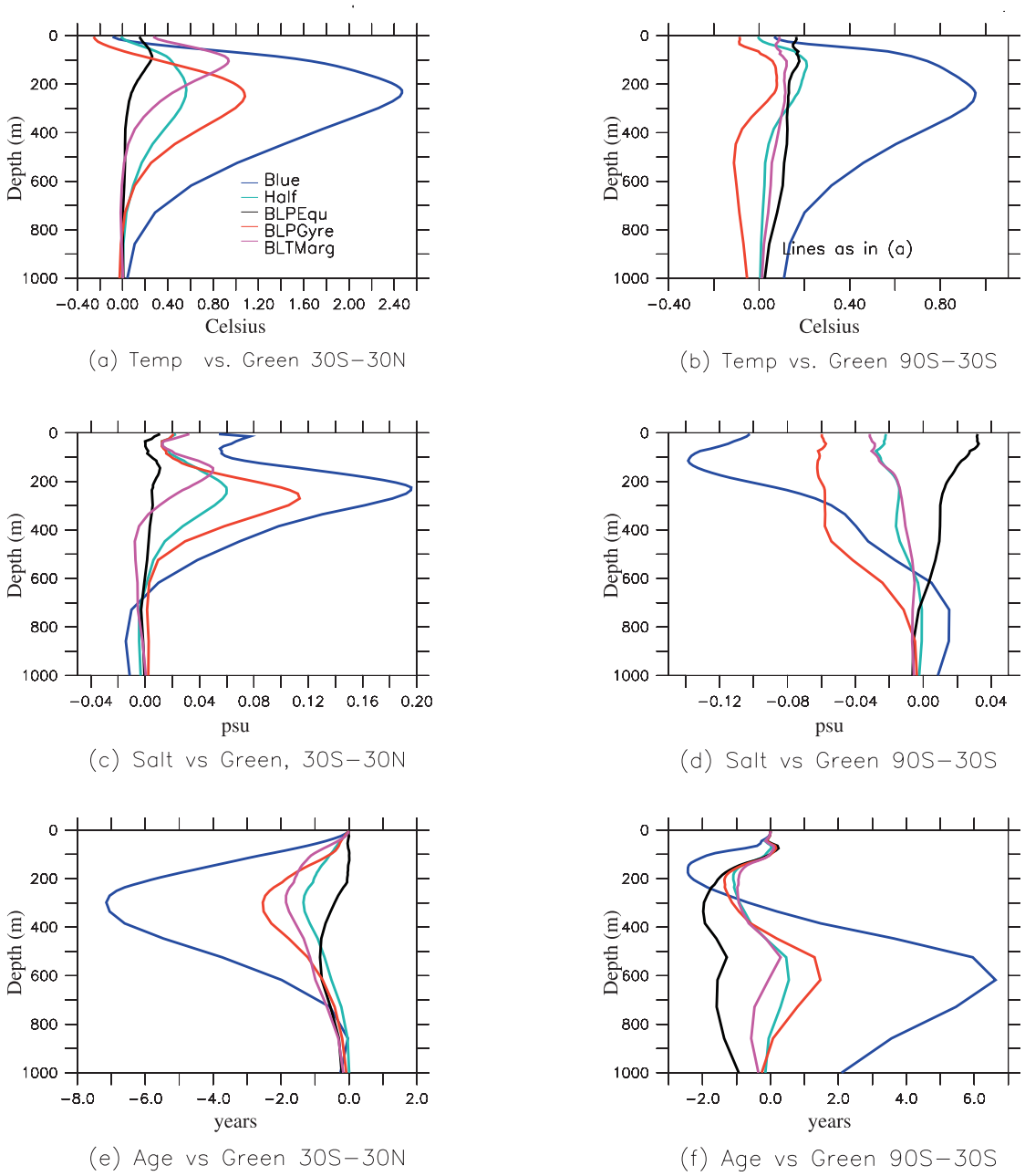

FIG. 5. Upper ocean changes in temperature (°C), salinity (psu), and ideal age (yr) relative to the Green simulation resulting from changes in ocean water clarity for years 81–120 of the simulations: (a) Temperature, 30°S–30°N; (b) temperature, 90°–30°S; (c) salinity, 30°S–30°N;. (d) salinity, 90°–30°S; (a) ideal age, 30°S–30°N. (b) Ideal age, 90°–30°S.

us cautious about overinterpreting these results, is that the effect is so large when heat is added to the eastern part of the shadow zones where SST biases are large. It is possible that this sensitivity may, in fact, be telling us something important about why models drift, rather than about the real world.

The additional heat added below the mixed layer also makes its way to the equator where it can also produce changes in the advective transport of heat. As shown in Fig. 6c, the average temperature of water moving eastward in the Equatorial Undercurrent (EUC) (defined as waters moving eastward with a velocity greater than 0.4 m s^{-1} within 3° of the equator) is much higher in the Blue run than in the Green. Increasing shortwave penetration along the equator or off the equator in the clear gyres produces changes in the temperature of

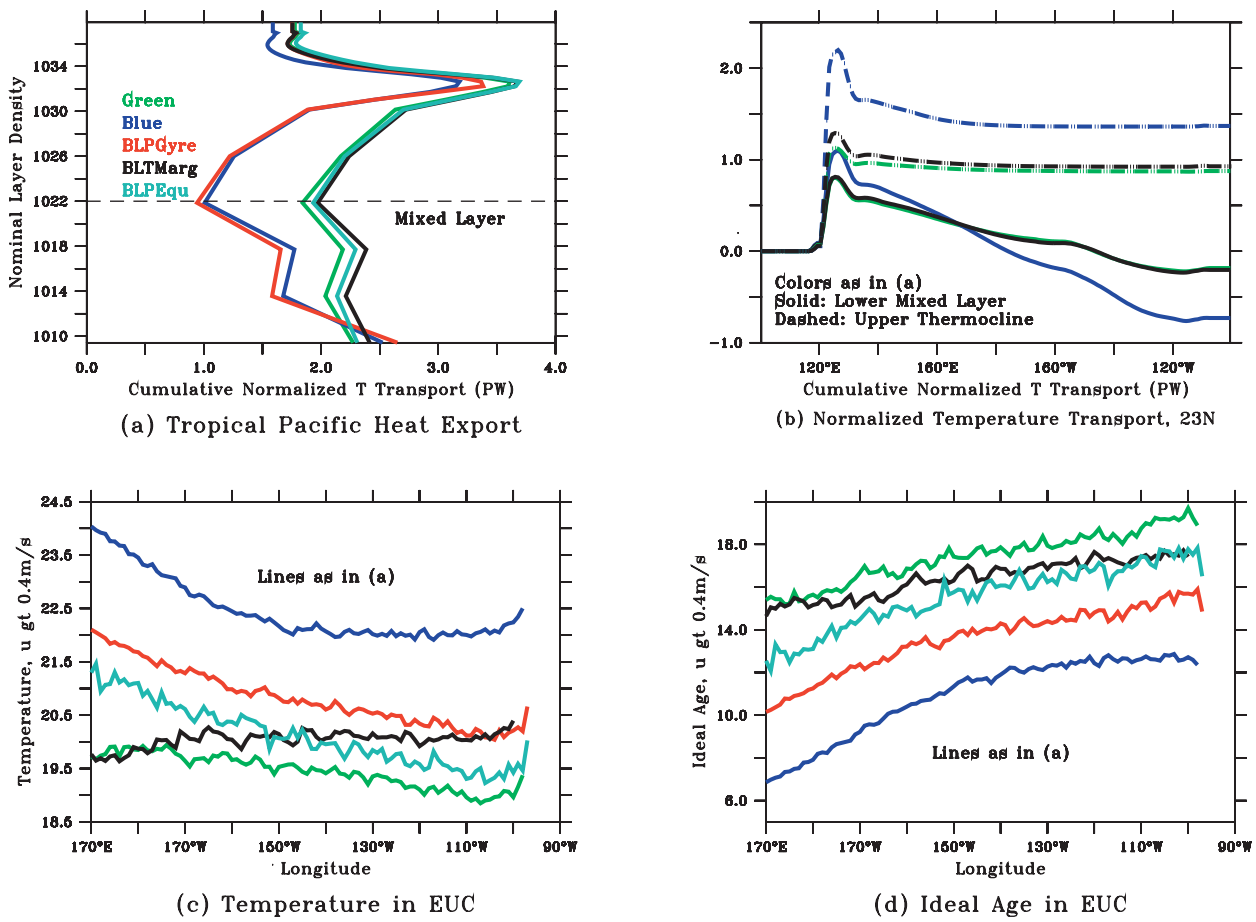

FIG. 6. Changes in heat transport and circulation associated with changing the shortwave penetration depth, years 41–120. (a) Cumulative normalized temperature transport in the vertical $Q_T^k = \sum_{n=0}^{k} \int \rho c_p v_n T_n h_n dx$ at 23°N in the model suite. Note the large differences between the Blue and BLPGyre simulations and the other simulations. (b) Cumulative normalized temperature transport in the meridional direction $Q_T(x) = \int_{x'=100\mathrm{E}}^{x} \sum_{n=ki}^{kf} \rho c_p v_n T_n h_n dx'$. Solid lines: cumulative transport in the lower mixed layer (layers 2–4); dashed lines: cumulative transport in the upper pycnocline. (c) Average temperature of water in the EUC defined as water moving eastward at a speed exceeding 0.4m s^{-1} within 3° of the equator. (d) Average ideal age of water in the EUC.

waters entering the EUC from the west. However, these changes are diluted by waters entering the EUC from the central Pacific. The BLTMarg run, by contrast, produces an increase in the temperatures of the waters that feed the EUC in the central and eastern Pacific. The changes in subsurface temperature are in part due to changes in the degree to which water in the upper thermocline exchanges with the mixed layer. This can be seen by looking at the changes in ideal age (Fig. 6d). This tracer drops from values of 15–17 yr in the Green run to 7–11 yr in the Blue run. The increases in EUC temperature are clearly associated with decreases in the age of water entering the undercurrent.

d. Tropics and subtropical wind-driven circulation

The changes in sea surface temperatures associated with increasing water clarity result in at least three major responses in the wind stress (Fig. 3). We will sketch the main features here (a more detailed analysis will be presented in Anderson et al. 2008, unpublished manuscript). The first is to increase convergence along the equator, strengthening the Hadley circulation and thus intensifying the zonal winds driven by this circulation. This can be seen most clearly in the BLPGyre run and is associated with the already clear gyre centers. Additionally, the changes in the upper-level winds produce changes in wave- activity fluxes, shifting the eddy-driven jets in midlatitudes equatorward so that the steep gradients in wind stress associated with the flanks of these jets intensify over the polar gyres. This effect is extremely pronounced over the subpolar North Pacific and Southern Ocean in the Blue run. Finally, the shift in convection associated with the warming of the eastern equatorial Pacific (as seen in the precipitation changes,

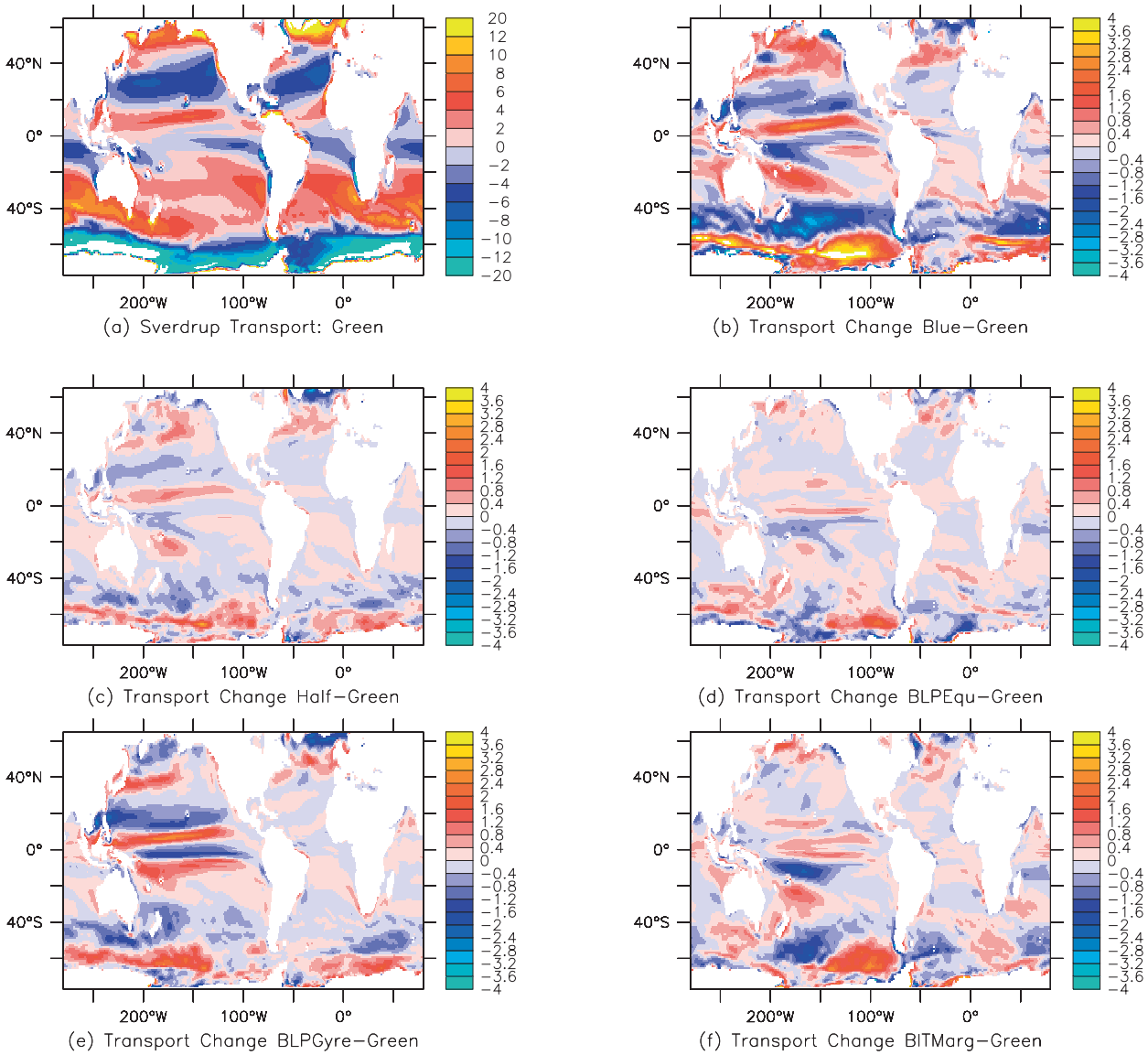

FIG. 7. Sverdrup transport ($m^2\ s^{-1}$) and its changes in the model suite for years 41–120 of the simulations: (a) Control transport from Green run (4 $m^2\ s^{-1}$ contour) and changes in transport (0.4 $m^2\ s^{-1}$ contour) for (b) Blue − Green, (c) Half − Green, (d) BLPEqu − Green, (e) BLPGyre − Green, and (f) BLTMarg − Green.

Fig. 4e) results in an El Niño–like wave pattern that has its expression in the intensification of the Aleutian low and an intensification of the low pressure over the Amundsen Sea. This last change is most strongly associated with the changes in water clarity in the BLTMarg simulation.

These changes in winds produce substantial changes in the wind stress curl and thus in the Sverdrup transport. Figures 7b–f show the changes in Sverdrup transport for the Blue − Green, BLPEqu − Green, Half − Green, BLPGyre − Green, and BLTMarg − Green simulations, with Fig. 7a showing the Sverdrup transport in the Green control case for comparison. Note that a change of 0.4 $m^2\ s^{-1}$ (the smallest colored contour interval) will correspond to a change of about 5 Sv (Sv ≡ $10^6\ m^3\ s^{-1}$) when integrated across the Pacific Ocean. Although the changes in Sverdrup transport are smaller than the mean transport, they are nonetheless significant.

These changes have a clear effect on the upper ocean circulation. The change in the streamfunction (derived from integrating the zonal velocity along 172°E in the top 38 layers, Fig. 8a) from Green to Blue shows a significant increase in the transport associated with the

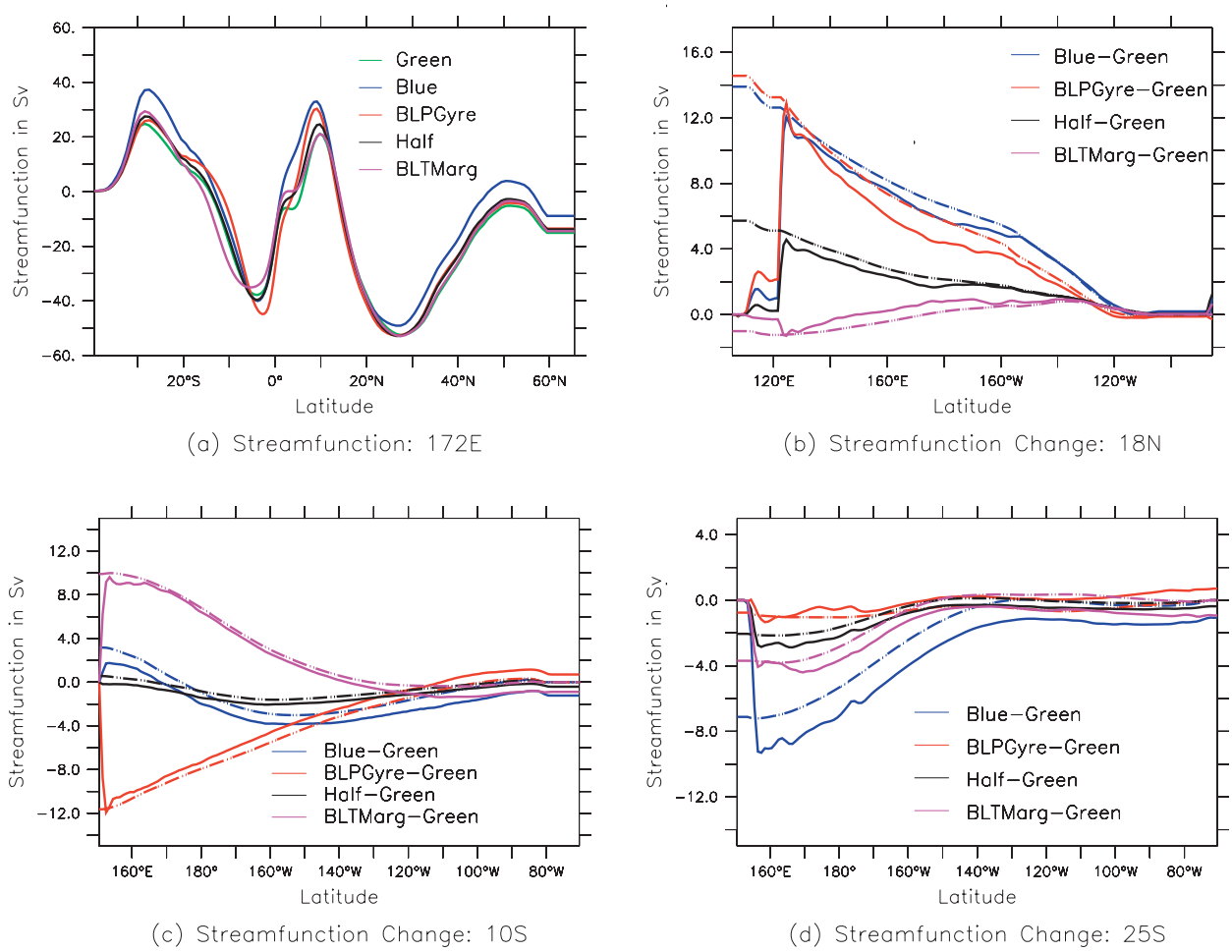

FIG. 8. Change in horizontal circulation associated with water clarity changes: dashed lines show integrated Sverdrup flux for years 41–120. All transports are in the top 38 layers (eliminating effects of bottom torques). (a) Eastward transport integrated along 172°E for four different models and northward transport integrated across the Pacific (b) at 18°N, (c) northward at 10°S, and (d) at 25°S.

North and South Equatorial Currents and their return flow in the EUC. Analysis of the differences in meridional transport at 18°N and 15° and 25°S (Figs. 8b–d) demonstrates that they can largely be attributed to the changes in Sverdrup transport. At 18°N (Fig. 8b), the changes are quite similar in shape for three of the models, differing primarily in magnitude, with the Blue, BLPGyre, and Half cases producing increases in the gyre circulation of 16, 12, and 6 Sv, respectively. This can be attributed to the strengthening of the Hadley cell north of the equator, resulting in an increase of the peak easterlies to the north. In the BLTMarg run, by contrast, there is much less strengthening of the northern Hadley cell, and a more negative wind stress curl in the eastern part of the gyre is compensated by a more positive wind stress curl in the west. The Blue − Green changes at this latitude are thus dominated by the changes in the relatively clear gyres.

This is not the case, however, at 10°S (Fig. 8c). In the BLPGyre case, the enhancement of the upwelling branch of the Hadley cell results in a strengthening and slight equatorward shift in the easterly jets to the north and south of the equator (though more so in the south than in the north). This in turn results in an equatorward shift of the subtropical gyre with an increase of 12 Sv in the gyre transport at 10°S. In the BLTMarg case, by contrast, there is a decrease in the wind stress curl in the western Pacific, associated with the movement of the southern rainband to the east, resulting in an increase in the northward transport at this latitude. The Blue and Half cases show a mixture of these two results, predicting essentially no increase in the gyre transport. Not all of the response can be attributed to local changes in the winds; there is also an offset of about 2 Sv, which is associated with a change in the Indonesian Throughflow.

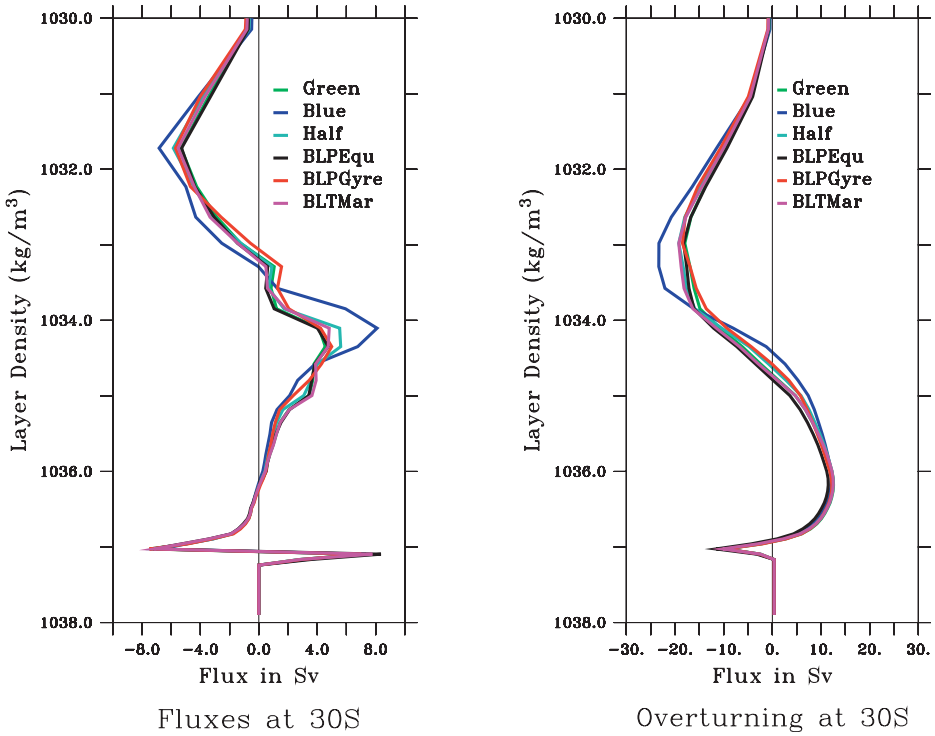

FIG. 9. Overturning at 30°S, years 41–120: (left) Fluxes (Sv) in each density class and (right) overturning streamfunction (Sv) integrated from lightest layers downward. Note the difference in transport between Blue and the other simulations.

Moving farther into the southern subtropics, we see that the dominant impact in Blue shifts to being associated with the tropical high-chlorophyll regions (Fig. 8d). At 25°S, both the Half and BLPGyre runs show a relatively small impact on wind stress curl and transport, while BLTMarg and Blue show a strong increase in northward Sverdrup transport associated with the eastward shift in precipitation (and the associated low pressure system) into the central Pacific.

e. Southern Ocean Subantarctic Mode Water and Antarctic Intermediate Water formation

Changes in wind stress magnitude and location over the Southern Ocean have been hypothesized to have the potential to cause significant changes in ocean ventilation and overturning (Toggweiler and Samuels 1993, 1998; Gnanadesikan and Hallberg 2000; Toggweiler et al. 2006). This is especially true in low-diffusion models where wind-driven Southern Ocean upwelling represents the dominant pathway by which dense deep waters are transformed into lighter surface waters (Toggweiler and Samuels 1998; Gnanadesikan 1999). The large changes in wind stress magnitude in this region would thus be expected to produce significant changes in overturning circulation, as shown in Fig. 9. The Half, BLPGyre, BLTMarg, BLPEqu, and Green runs are essentially identical, with 18 Sv of light and 22–23 Sv of dense water entering the Southern Ocean and 10–11 Sv of abyssal and 30 Sv of intermediate and mode waters leaving the region. The Blue run is significantly different. The supply of light water associated with the subtropical gyres increases by almost 40% to 25 Sv. The northward flow of mode and intermediate waters also increases, to about 37 Sv. As a result, the mode and intermediate waters become even more dominated by the lighter water mass classes.

The fact that the overturning is so different for the Blue run raises the question of the role played by extratropical ocean color, which we have largely ignored until now. By trapping heat near the surface, extratropical solar absorption will tend to raise summertime temperatures while lowering wintertime temperatures. Such a temperature change could have one of two impacts. First, it could have a direct impact on water mass transformation. To explain the changes seen here, we would expect that the Green run would have significantly less wintertime transformation of dense water than the Blue. Second, the changes in seasonal temperature could have an impact on the wind stress field, resulting in a change in the gyre circulation. Analysis of the transport of water lighter than

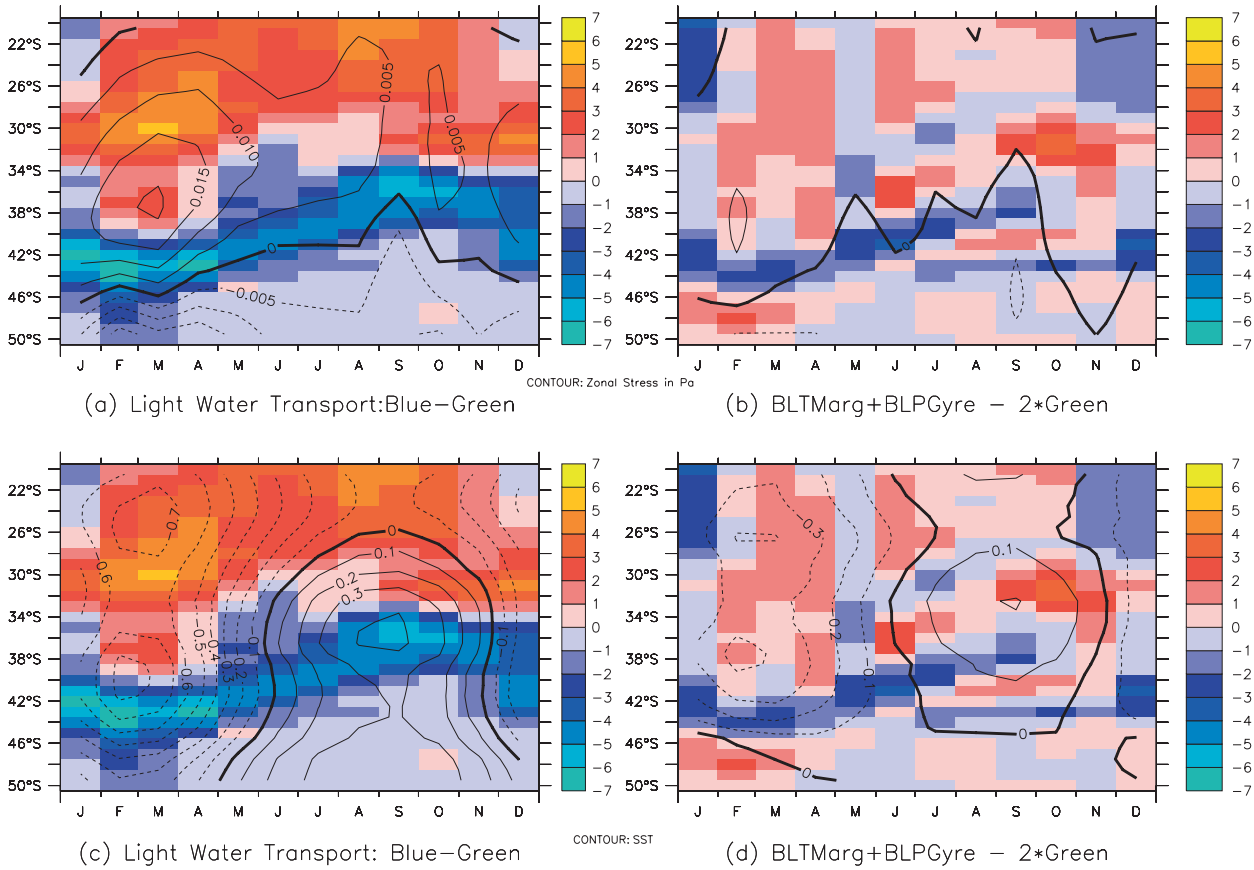

FIG. 10. Changes in the northward transport of light water related to surface quantities over the course of the year: climatology shown for years 41–120. (a) Zonally integrated light water transport change (Sv) (colors) and zonally averaged surface wind stress change (Pa) (contours) between the Blue and Green runs. Note how light water transport change follows wind stress changes. (b) As in (a), but for (BLPGyre − Green) + (BLTMarg − Green). Note that the additional northward transport is not seen, nor are the changes in zonally integrated wind stress. (c) As in (a), but with contours of zonally averaged SST change overlaid. (d) As in (b), but with contours of zonally averaged SST change overlaid.

1034.5 (Fig. 10a) shows that there is more creation of this water within the Southern Ocean throughout the year (suggesting that it is not the impact of temperature alone that matters). The location where the additional creation of light water occurs seems to be related to the wind stress field. The increased southward transport of light water corresponds to regions where the zonal winds are adding negative curl. The added curl is more than sufficient to explain the changes in light water transport. In February the zonally averaged wind stress increases by 0.02 Pa at 38°S and decreases by an equivalent amount at 50°S. The Sverdrup transport associated with such a change is -1.7 m^2 s^{-1} at 42°S: 52 Sv when integrated around the globe, compared to an additional 6 Sv of light water being transported to the south. Similarly, the increased northward transport corresponds to regions where the zonal winds are adding increased positive curl.

The BLPGyre and BLTMarg perturbations, when added together, do produce a slightly enhanced southward transport of this light water, but do not show the enhancement in northward transport (Figs. 10b). Neither do these low-latitude perturbations reproduce the relatively large changes in the wind stress (up to 0.02 Pa in the zonal mean in some months) or in SST (changes of up to 0.7°C). This suggests that it is the indirect effect of extratropical temperature changes on the wind stress curl that is most important for changing the Southern Hemisphere overturning. The fact that the Half run does not show such a large impact suggests that the temperature changes involved may result from changes in convection, which would involve crossing some threshold.

4. Discussion

Although the use of perturbations in which chlorophyll is completely removed is (hopefully!) extreme, the results presented here do raise some interesting connections to

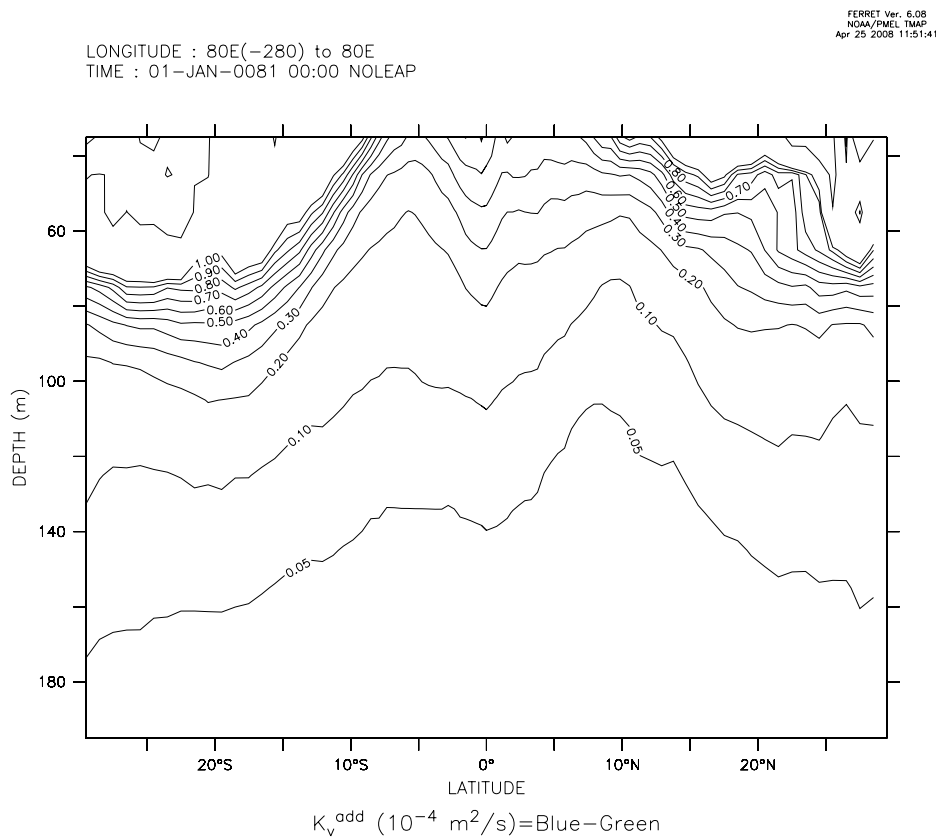

FIG. 11. Diffusion coefficient (10^{-4} m^2 s^{-1}) that would produce a vertical heat flux equivalent to the additional shortwave flux caused by changing k_{bg} from the value used in Green to the value used in Blue.

other issues in earth system modeling. The first of these involves ocean physics. Because changing the profile of solar absorption can be seen as similar in effect to changes in the background mixing coefficient, moving heat vertically in the water column, our results suggest that the climate system could be very sensitive to the amount of mixing below the mixed layer. One can get a rough sense of how important this is by computing the diffusive coefficient required to match the additional shortwave flux:

$$K_v^{\mathrm{add}} = \Delta \mathrm{SW}/(\rho c_p \partial T/\partial z), \tag{3}$$

where ΔSW is the change in downwelling shortwave flux, ρ the density, c_p the specific heat, and $\partial T/\partial z$ is the background stratification. We computed this quantity using the zonally averaged $\partial T/\partial z$ from the Green simulation and computed ΔSW using the difference between the zonally averaged flux from the Green simulation and the zonally averaged flux using the same incoming radiation as in Green but using the penetration depth of 43 m as in Blue. By computing the change in flux in this manner we are able to estimate the change in flux due to changing penetration alone, without considering coupled feedbacks.

As seen in Fig. 11, the additional diffusion required to change the vertical heat flux as much as removing ocean color is extremely small, of order 0.05–0.2 ($\times$ 10^{-4}) m^2 s^{-1} for most depths below 100 m and less than 10^{-4} m^2 s^{-1} below about 60 m everywhere. This suggests that models could be very sensitive to small changes in either numerical of explicit diffusivity immediately below the mixed layer base. Most coupled models, including ours, assume that once outside the zone of active mixing, the mixing coefficient immediately drops to values typical of the interior [0.1–0.15 ($\times$ 10^{-4} m^2 s^{-1})]. However, it is known that the zone immediately below the mixed layer has different internal wave properties and could therefore exhibit different mixing behavior. For example, Anis and Singhal (2006) show microstructure measurements in a freshwater lake in which the pycnocline was well defined. While they do see a marked difference between high mixing coefficients within the mixed layer and the low mixing coefficients in the pycnocline, they

also find patches of high vertical diffusion below the mixed layer. Our results suggest that much more attention should be paid to the impact of such near-surface turbulence patches.

Our results also suggest the possibility of some interesting coupling between the iron cycle and circulation. Iron is an important micronutrient for phytoplankton. Iron supply to the oceans is largely associated with airborne mineral dust, with the Sahara accounting for a large fraction of this supply (Li et al. 2008). These dust sources have changed markedly over time, particularly as a result of Saharan desertification. Additionally, increases in sulfur dioxide pollution (which, as discussed in Fan et al. 2006, acts to increase the solubility of iron in dust) would be expected to increase chlorophyll concentrations in the North Pacific.

5. Summary and conclusions

It is increasingly clear that ocean biology is far from being a passive player in the climate system. Our results show that changing water clarity can produce significant changes in the climate and circulation. This paper shows that different regions play significantly different roles in changing the pattern of surface temperature and circulation. Increasing shortwave penetration along the equator produces relatively small changes in surface temperature and circulation, with some additional warming to the south of the equator. Increasing penetration in the low-chlorophyll subtropical gyres results in strong cooling off the equator and weak warming along the equator, with the potential to induce equatorward shifts of the subtropical gyres that can result in transport changes up to 20 Sv. Increasing penetration in the high-chlorophyll tropical margins has a very large impact on the temperatures throughout the shadow zones and at the surface, highlighting the potential climatic importance of these regions. The fact that these changes are larger than in previous simulations suggests that it is the modulation of heating at significant depths (100–200 m) that is particularly important.

The sensitivity of the results to shortwave absorption in regions with relatively low levels of chlorophyll further highlights the importance of properly understanding the dynamics of light absorption in these regions. Parameterizations of water clarity have tended to use chlorophyll-*a* (Morel 1988), in large part because in situ measurements of this quantity are relatively easy to make. However, it has become abundantly clear in recent years that a significant fraction of shortwave absorption is due to constituents such as chromophoric dissolved organic matter (Siegel and Michaels 1996; Siegel et al. 2005; Nelson et al. 2007; Morel et al. 2007), which can have radically different behavior than chlorophyll-*a*. This work suggests that a detailed examination of the differing impacts of different absorbers on a regional basis could reveal hitherto unsuspected feedbacks between biological cycling and the climate system.

Acknowledgments. The authors thank the Geophysical Fluid Dynamics Laboratory for support of these runs. WGA was supported by NASA under the ECCO consortium (Grant NNG06GC28G) and the Interdisciplinary Science initiative (Grant NNX07AL801G). We thank Steve Griffies, Laura Jackson, and Andrew Wittenberg for reviewing this manuscript; Bonnie Samuels for help with the model setup and for running the control simulation; and Bob Hallberg, John Dunne, and Tony Rosati for useful discussions. Comments from Jack Barth and two anonymous reviewers are gratefully acknowledged.

REFERENCES

Anderson, W. G., A. Gnanadesikan, R. W. Hallberg, J. P. Dunne, and B. L. Samuels, 2007: Impact of ocean color on the maintenance of the Pacific Cold Tongue. *Geophys. Res. Lett.,* **34,** L11609, doi:10.1029/2007GL030100.

Anis, A., and M. A. Singhal, 2006: Mixing in the surface boundary layer of a tropical freshwater reservoir. *J. Mar. Syst.,* **63,** 225–243.

Ballabrera-Poy, J., R. Murtugudde, R.-H. Zhang, and A. Busalucchi, 2007: Coupled ocean–atmosphere response to seasonal modulation of ocean color: Impact on interannual climate modulations in the tropical Pacific. *J. Climate,* **20,** 353–374.

Delworth, T., and Coauthors, 2006: GFDL CM2 global coupled climate models. Part I: Formulation and simulation characteristics. *J. Climate,* **19,** 643–674.

Fan, S. M., W. J. Moxim, and H. Levy II, 2006: Aeolian input of bioavailable iron to the ocean. *Geophys. Res. Lett.,* **33,** L07062, doi:10.1029/2005GL024852.

Federov, A., P. Dekens, M. McCarthy, A. C. Ravelo, P. B. DeMenocal, M. Barreiro, R. C. Pacanowski, and S. G. H. Philander, 2006: The Pliocene paradox—Mechanisms for a permanent El Niño. *Science,* **312,** 1485–1489.

Gent, P., and J. C. McWilliams, 1990: Isopycnal mixing in ocean models. *J. Phys. Oceanogr.,* **20,** 150–155.

Gnanadesikan, A., 1999: A simple theory for the structure of the oceanic pycnocline. *Science,* **283,** 2077–2079.

——, and R. W. Hallberg, 2000: On the relationship of the Circumpolar Current to Southern Hemisphere winds in large-scale ocean models. *J. Phys. Oceanogr.,* **30,** 2013–2034.

——, J. L. Russell, and F. Zeng, 2007: How does ocean ventilation change under global warming? *Ocean Sci.,* **3,** 43–53.

Griffies, S., and Coauthors, 2009: Coordinated Ocean-ice Reference Experiments (CORES). *Ocean Modell.,* **29,** 1–46.

Hallberg, R. W., 2005: A thermobaric instability of Lagrangian vertical coordinate ocean models. *Ocean Modell.,* **8,** 279–300.

Harrison, M. J., and R. W. Hallberg, 2008: Pacific subtropical cell response to reduced equatorial dissipation. *J. Phys. Oceanogr.,* **38,** 1894–1912.

Jerlov, N. G., 1976: *Marine Optics.* Elsevier, 231 pp.

Karl, D. M., R. R. Bidigare, and R. M. Letelier, 2001: Long-term changes in phytoplankton community structure and productivity in the North Pacific Subtropical Gyre—The domain shift hypothesis. *Deep-Sea Res. II,* **48,** 1449–1470.

Lengaigne, M., C. Menkes, O. Aumont, T. Gorgues, L. Bopp, J.-M. Andre, and G. Madec, 2007: Influence of the oceanic biology on the tropical Pacific climate in a coupled general circulation model. *Climate Dyn.,* **28,** 503–516.

Lewis, M. R., M. E. Carr, G. C. Feldman, W. Esaias, and C. McClain, 1990: Influence of penetrating solar radiation on the heat budget of the equatorial Pacific Ocean. *Nature,* **347,** 543–545.

Li, F., P. Ginoux, and V. Ramaswamy, 2008: Distribution, transport, and deposition of mineral dust in the Southern Ocean and Antarctica: Contribution of major sources. *J. Geophys. Res.,* **113,** D10207, doi:10.1029/2007JD009190.

Luyten, J. L., J. Pedlosky, and H. M. Stommel, 1983: The ventilated thermocline. *J. Phys. Oceanogr.,* **13,** 292–309.

Manizza, M., C. Le Quere, A. J. Watson, and E. T. Buitenhuis, 2005: Bio-optical feedbacks among phytoplankton, upper ocean physics and sea-ice in a global model. *Geophys. Res. Lett.,* **32,** L05603, doi:10.1029/2004GL020778.

Marzeion, B., A. Timmermann, R. Murtugudde, and F. F. Jin, 2005: Biophysical feedbacks in the tropical Pacific. *J. Climate,* **18,** 58–70.

McClain, C. R., G. C. Feldman, and S. B. Hooker, 2004: An overview of the SeaWiFS project and strategies for producing a climate research quality global ocean bio-optical time series. *Deep-Sea Res. II,* **51,** 5–42.

Milly, P. C. D., and A. B. Shmakin, 2002: Global modeling of land, water, and energy balances. *J. Hydrometeor.,* **3,** 283–299.

Moore, J., S. C. Doney, J. Kleypas, D. Glover, and I. Y. Fung, 2002: An intermediate complexity marine ecosystem model for the global domain. *Deep-Sea Res.,* **49B,** 403–462.

Morel, A., 1988: Optical modeling of the upper ocean in relation to its biogenous matter content (Case I Waters). *J. Geophys. Res.,* **93,** 10 749–10 768.

——, H. Claustre, D. Antoine, and B. Gentili, 2007: Natural variability of bio-optical properties in Case I waters: Attenuation and reflectance in the visible and near-UV spectral domains, as observed in South Pacific and Mediterranean waters. *Biogeosciences,* **4,** 913–925.

Murtugudde, R., J. Beauchamp, C. R. McClain, M. Lewis, and A. Busalacchi, 2002: Effects of penetrative radiation on the upper tropical ocean circulation. *J. Climate,* **15,** 470–486.

Nakamoto, S., S. P. Kumar, J. M. Oberhuber, J. Ishizaka, K. Muneyama, and R. Frouin, 2001: Response of the equatorial Pacific to chlorophyll pigment in a mixed layer isopycnal ocean general circulation model. *Geophys. Res. Lett.,* **28,** 2021–2024.

Nelson, N. B., D. A. Siegel, C. A. Carlson, C. Swan, W. M. Smethie, and S. Khatiawala, 2007: Hydrography of chromophoric dissolved organic matter in the North Atlantic. *Deep-Sea Res. I,* **54,** 710–731.

Paytan, A., and E. M. Griffith, 2007: Marine barite: Recorder of variations in ocean export productivity. *Deep-Sea Res. II,* **54,** 687–705, doi:10.1016/j.dsr2.2007.01.007.

Polovina, J. J., E. A. Howell, and M. Abecassis, 2008: Ocean's least productive waters are expanding. *Geophys. Res. Lett.,* **35,** L03618, doi:10.1029/2007GL031745.

Reichler, T., and J. Kim, 2008: How well do coupled climate models simulate today's climate? *Bull. Amer. Meteor. Soc.,* **89,** 303–311.

Schneider, E., and Z. Zhu, 1998: Sensitivity of the simulated annual cycle of sea surface temperature in the equatorial Pacific to sunlight parameterization. *J. Climate,* **11,** 1932–1950.

Shell, K. M., S. Nakamoto, and R. C. Somerville, 2003: Atmospheric response to solar radiation absorbed by phytoplankton. *J. Geophys. Res.,* **108,** 4445, doi:10.1029/2003JD003440.

Siegel, D. A., and A. F. Michaels, 1996: Quantification of nonalgal light attenuation in the Sargasso Sea: Implications for biogeochemistry and remote sensing. *Deep-Sea Res. II,* **43,** 321–345.

——, R. R. Bidigare, and Y. Zhou, 1995: Solar radiation, phytoplankton pigments and the radiant heating of the equatorial Pacific warm pool. *J. Geophys. Res.,* **100,** 4885–4891.

——, S. Maritorona, N. B. Nelson, and M. J. Behrenfeld, 2005: Independence and interdependencies among global ocean color properties: Reassessing the bio-optical assumption. *J. Geophys. Res.,* **110,** C07011, doi:10.1029/2004JC002527.

Stramska, M., and T. D. Dickey, 1993: Phytoplankton bloom and the vertical thermal structure of the upper ocean. *J. Mar. Res.,* **51,** 819–842.

Strutton, P. G., and F. P. Chavez, 2004: Biological heating in the equatorial Pacific: Observed variability and potential for real-time calculation. *J. Climate,* **17,** 1097–1109.

Sweeney, C., A. Gnanadesikan, S. M. Griffies, M. J. Harrison, A. Rosati, and B. L. Samuels, 2005: Impacts of shortwave penetration depth on large-scale ocean-circulation and heat transport. *J. Phys. Oceanogr.,* **35,** 1103–1119.

Timmermann, A., and F.-F. Jin, 2002: Phytoplankton influences on tropical climate. *Geophys. Res. Lett.,* **29,** 2104, doi:10.10129/2002GL015434.

Toggweiler, J. R., and B. L. Samuels, 1993: Is the magnitude of the deep outflow from the Atlantic Ocean actually governed by Southern Hemisphere winds? *The Global Carbon Cycle.,* Springer-Verlag, 303–331.

——, and B. Samuels, 1998: On the ocean's large-scale circulation near the limit of no vertical mixing. *J. Phys. Oceanogr.,* **28,** 1832–1852.

——, J. L. Russell, and S. R. Carson, 2006: Midlatitude westerlies, atmospheric CO_2, and climate change during the ice ages. *Paleoceanography,* **21,** PA2005, doi:10.1029/2005PA001154.

Van Oldenburgh, G. J., S. Y. Philip, and M. Collins, 2005: El Niño in a changing climate: A multi-model study. *Ocean Sci.,* **1,** 81–95.

Wetzel, P., E. Maeier-Reimer, M. Botzet, J. Jungclaus, N. Keenlyside, and M. Latif, 2006: Effects of ocean biology on the penetrative radiation in a coupled climate model. *J. Climate,* **19,** 3973–3987.

Winton, M., R. W. Hallberg, and A. Gnanadesikan, 1998: Simulation of density-driven downslope flow in z-coordinate ocean models. *J. Phys. Oceanogr.,* **28,** 2163–2174.